Electronic Supplementary Information

Multiporous Structure Formation in Three-Way Catalysts Particles for Enhanced Catalytic Performance

*Duhaul Biqal Kautsar[1], Phong Hoai Le[1], Kosuke Kondo[1], Kiet Le Anh Cao[1], Eka Lutfi Septiani[1], Tomoyuki Hirano[1], and Takashi Ogi[1]**

[1]Chemical Engineering Program, Department of Advanced Science and Engineering, Graduate School of Advanced Science and Engineering, Hiroshima University, 1-4-1 Kagamiyama, Higashi Hiroshima, Hiroshima 739-8527, Japan

*Corresponding author: Takashi Ogi, ogit@hiroshima-u.ac.jp

Tel/Fax: +81-82-424-3765

KEYWORDS: three-way catalysts, CO oxidation, Multiporous structure, spray process, nanostructured particles.

Contents:

1. TWC nanoparticles

The three-way catalyst (TWC) used in this study is a commercial catalyst supplied by Mitsui Mining & Smelting Co., Ltd., Japan, and was employed as received without further modification. According to the supplier's specification, this material contains platinum group metals, specifically Pd (1.26 wt%) and Rh (0.21 wt%), which serve as the active catalytic components, supported on a mixed oxide system comprising CeO_2 (18.4 wt%), ZrO_2 (26.2 wt%), Al_2O_3 (47.82 wt%), La_2O_3 (1.81 wt%), Nd_2O_3 (2.0 wt%), and La (1.48 wt%). In this formulation, CeO_2–ZrO_2 provides oxygen storage, while Al_2O_3 acts as a high-surface-area stabilizing support. SEM (**Fig. S1a**) and TEM (**Fig. S1b1**) images indicate that the TWC nanoparticles form irregular clusters with rough surface textures, and previous studies have shown that the overall nanoparticle size is in the range of 8–10 nm.[1–3] Furthermore, TEM-EDS mapping (**Fig. S1b2-5**) of representative elements, including Ce, Zr, Al, and Pd, was conducted to investigate their distribution within the TWC nanoparticles. The results demonstrate that all these components are uniformly distributed throughout the catalyst nanoparticles.

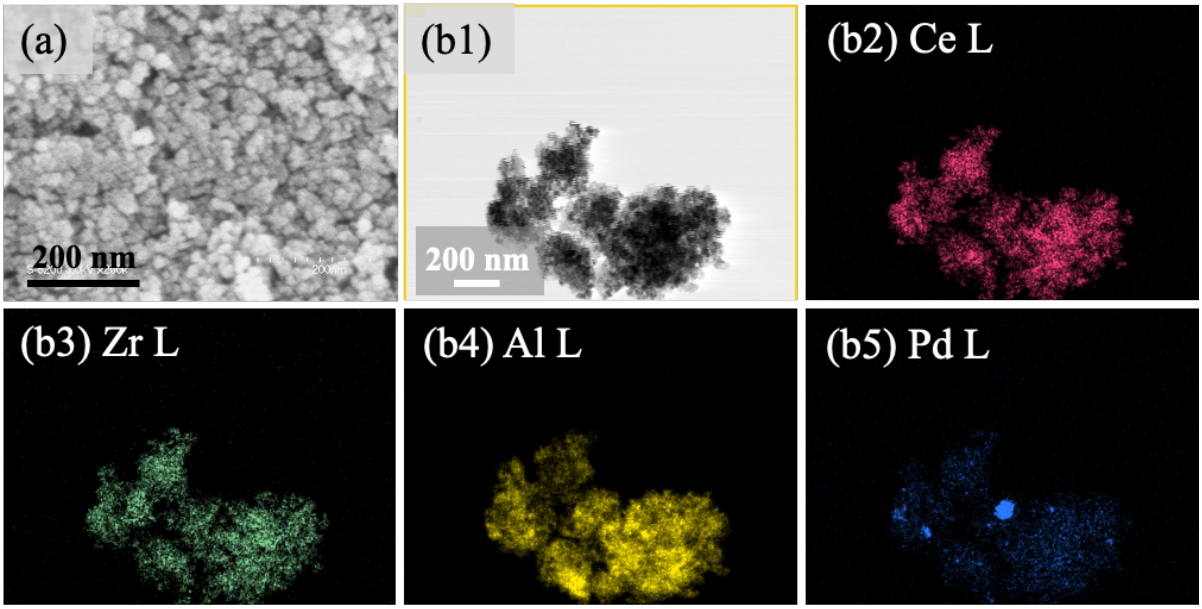

Fig. S1 (a) SEM, (b1) TEM image and (b2-5) and EDS elemental mapping of TWC nanoparticles for (b2) Ce, (b3) Zr, (b4) Al, and (b5) Pd.

2. Synthesis process of multiporous TWC particles

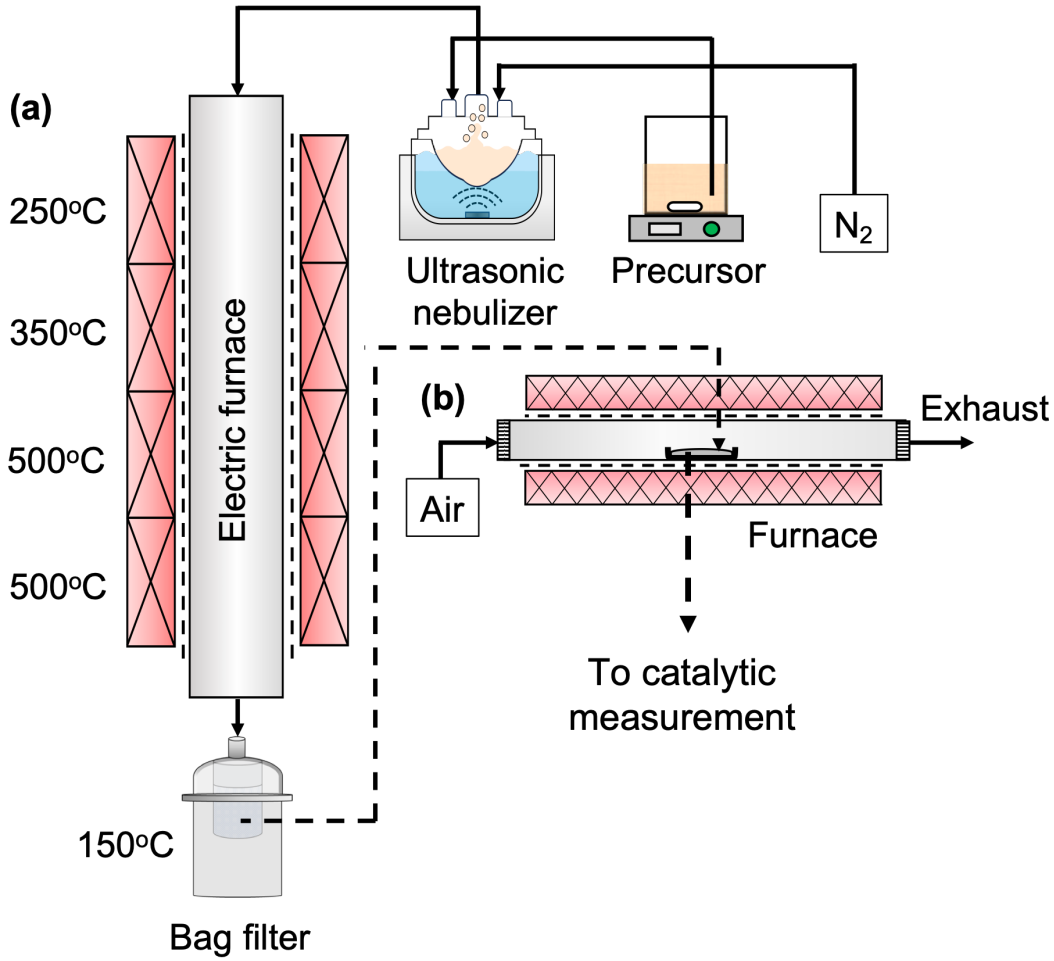

Fig. S2 Experimental setup of (a) vertical furnace spray and (b) annealing process.

3. Morphology of PMMA template particles

Fig. S3 shows the morphology of the PMMA particles used in this study. These particles are of the same type and size as those used in the previous study.[2]

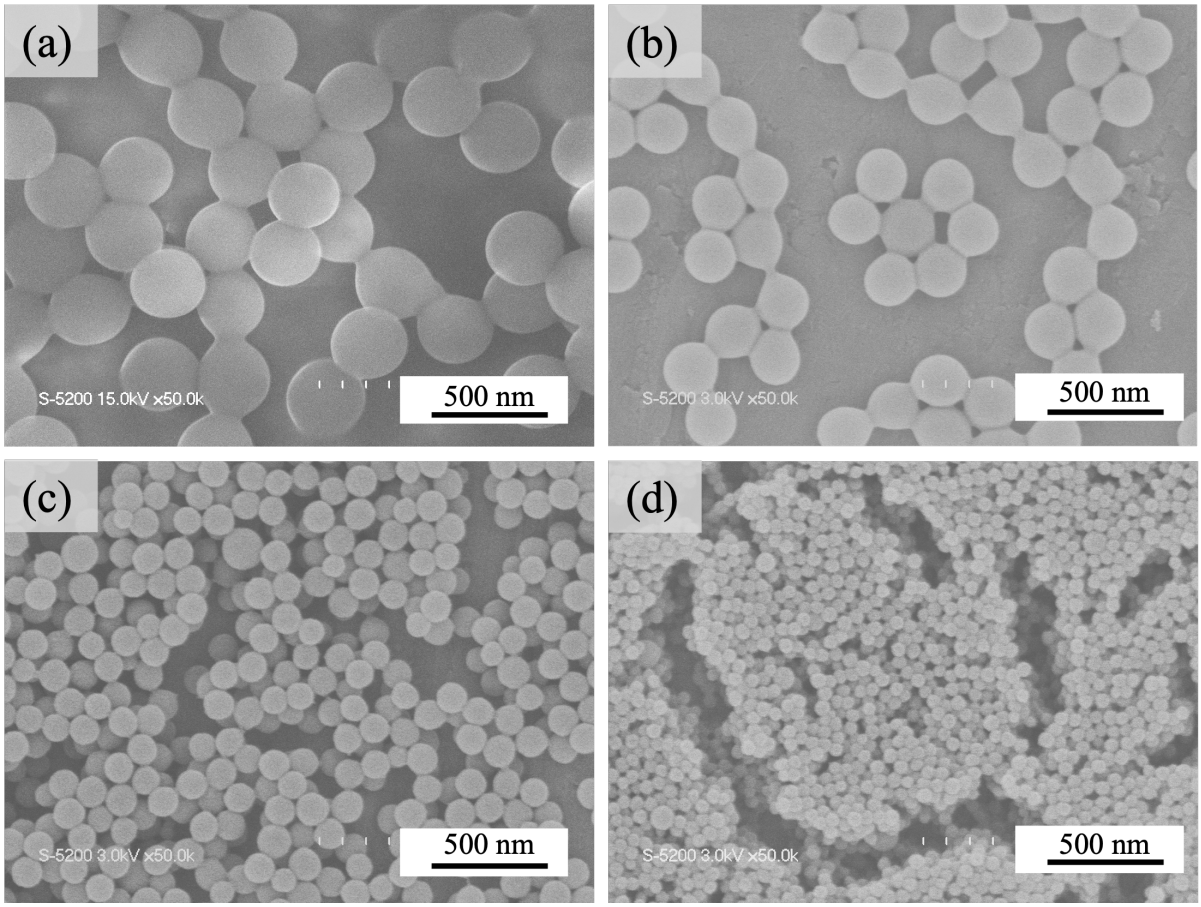

Fig. S3 SEM images of PMMA particles with the size of (a) 381 nm, (b) 242 nm, (c) 138 nm, and (d) 61 nm.

4. Particle size of single and multiporous TWC particles

To predict the particle size, the given densities of TWC (4.83 g/cm^3) and PMMA (1.18 g/cm^3) are applied. Furthermore, the droplet diameter is 5 µm,[4,5] while porosity is assumed to be 42%, based on the typical values for real particle packings.[6]

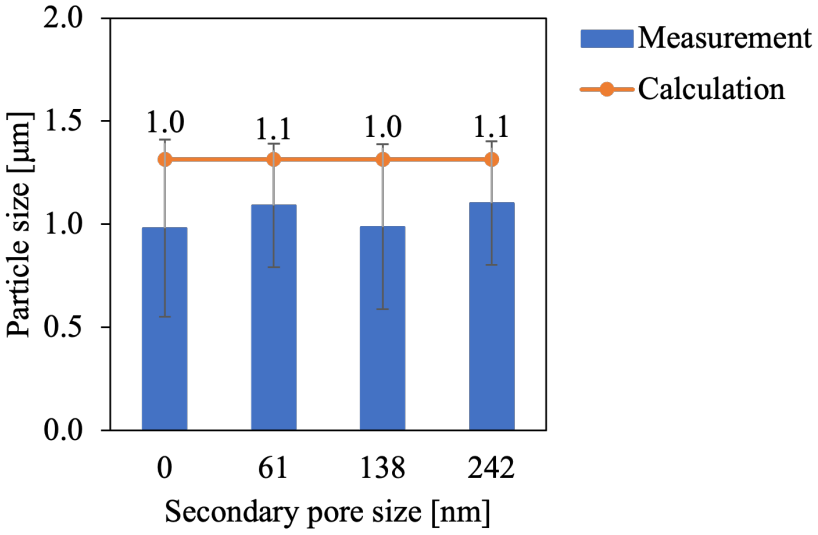

Fig. S4 The effect of secondary pore size to the particle size of multiporous TWC particles.

5. Mesopores formation from TWC nanoparticles packing arrangement

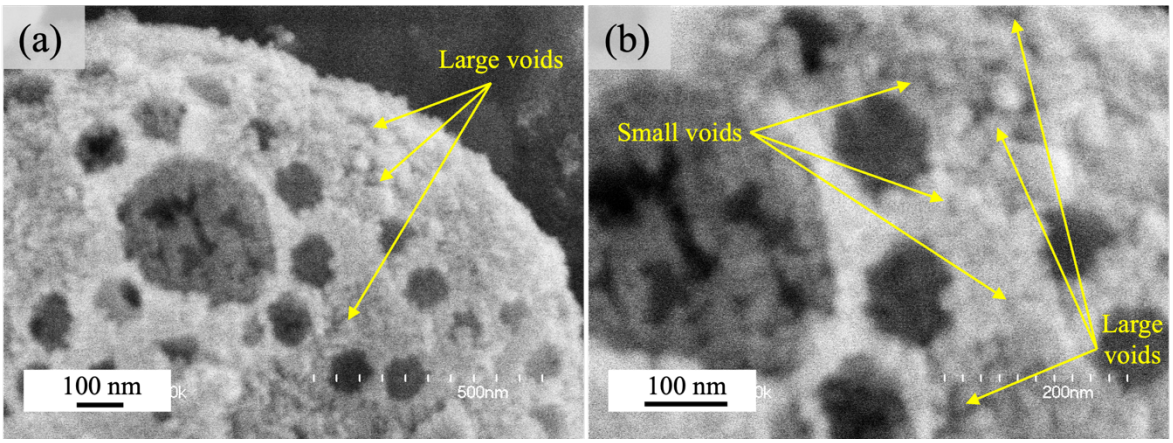

Fig. S5 SEM images of multiporous TWC particles from 0.5P381–0.5P138 sample at (a) 100k and (b) 200k magnifications.

6. Macroporosity of single and multiporous TWC particles

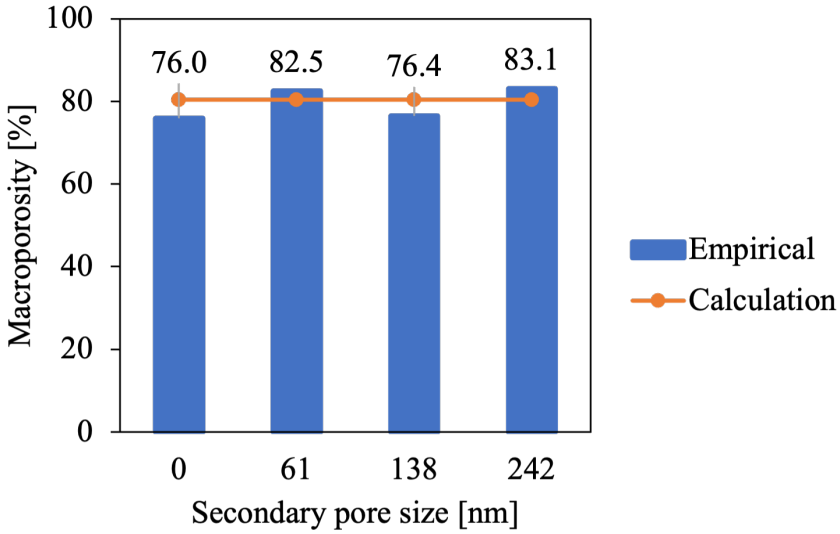

Fig. S6 The effect of secondary pore size to the macroporosity of multiporous TWC particles.

7. Crystallinity of single and multiporous TWC particles

The XRD patterns of the sample were compared with references from the Crystallography Open Database (COD), where Al_2O_3 was indexed using COD 1101168 and $CeZrO_4$ using COD 1521415 (**Fig. S7**). The correspondence between the experimental peaks and these COD reference patterns indicates that the synthesized material predominantly consists of a multiphase structure of Al_2O_3 and $CeZrO_4$, with no additional crystalline phases from other metal oxides observed. This absence can be attributed to the presence of other metals, such as La_2O_3 and Nd_2O_3, as well as active components from platinum-group metals (Pd and Rh), which are present at very low loadings (≤ 2 wt%) compared to the support, making their signals too weak to be detected by XRD. Additionally, these metals are highly dispersed on the support surface as nanoclusters or even atomically dispersed species. Consequently, only the main crystalline phases, Al_2O_3 and $CeZrO_4$, are visible in the diffraction patterns.

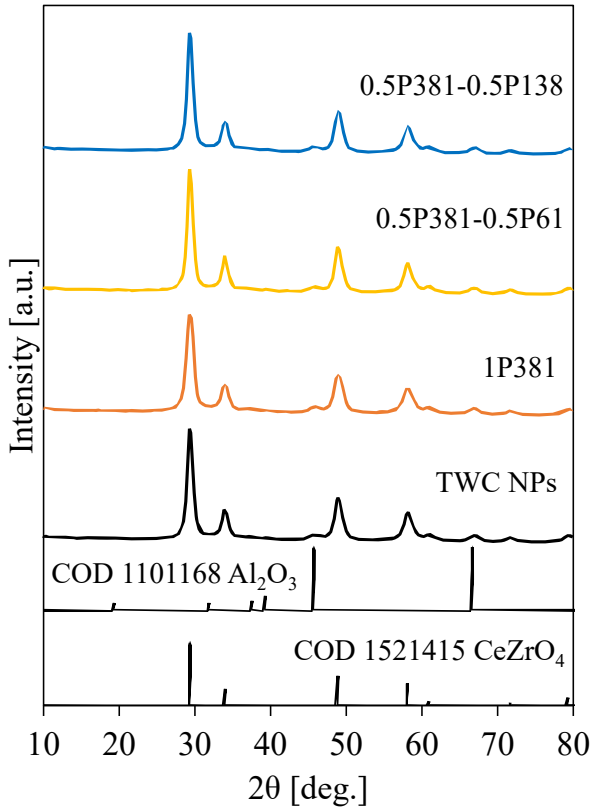

Fig. S7 XRD patterns of multiporous TWC particles.

8. T_{90} investigation of multiporous TWC particles

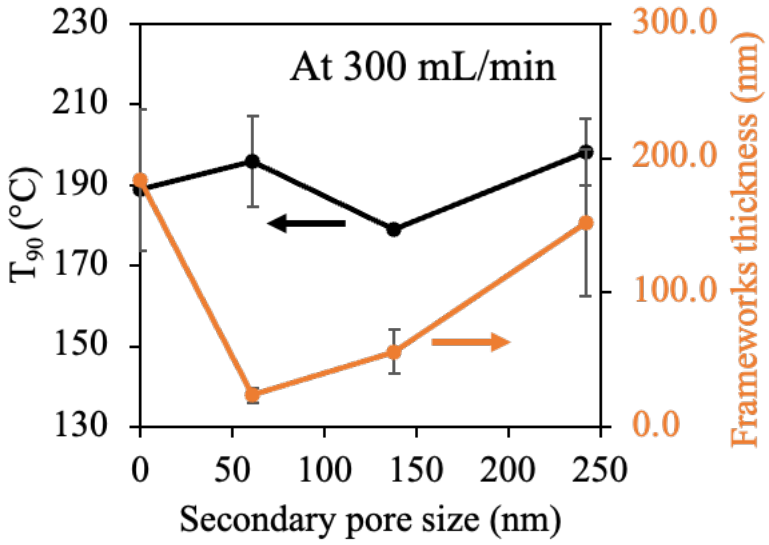

Fig. S8 T_{90} performance of multiporous TWC particles and their relationship with framework thickness.

9. TEM EDS analysis of multiporous TWC particles

TEM images of multiporous TWC particles from 0.5P381-0.5P138 sample show that the primary and secondary macropores are observed to be distributed within the internal part of the particles (**Fig. S9a1**). The EDS elemental mapping further reveals that Ce, Zr, Al, Pd, and O are distributed across the particle framework (**Fig S9a2-a6**). To further confirm the distribution of TWC components in this multiporous samples, a comparison with particles of a different morphology, particularly the aggregate structure (AGT1 sample), was also conducted (**Fig. S9b1**). Aggregate particles were chosen because the multiporous TWC framework is originally formed from aggregated TWC nanoparticles. Thus, the aggregate particles serve as a representative model without the influence of pore structures. The results show that the elemental distribution in the aggregate-structured TWC is also uniformly distributed throughout the entire particles (**Fig S9b2-b6**). Moreover, the EDS line scan analysis further supports this observation, showing signals of Ce, Zr, Al, Pd, and O in both the external and internal regions across the scanned area of the multiporous (**Fig. S10a**) and aggregate (**Fig. S10b**) TWC particles. The distribution of TWC components remains unchanged from the nanoparticle form to the aggregate and multiporous structures, indicating that the nanostructuring process achieved through the spray-drying method does not alter the overall elemental distribution within the TWC particles.

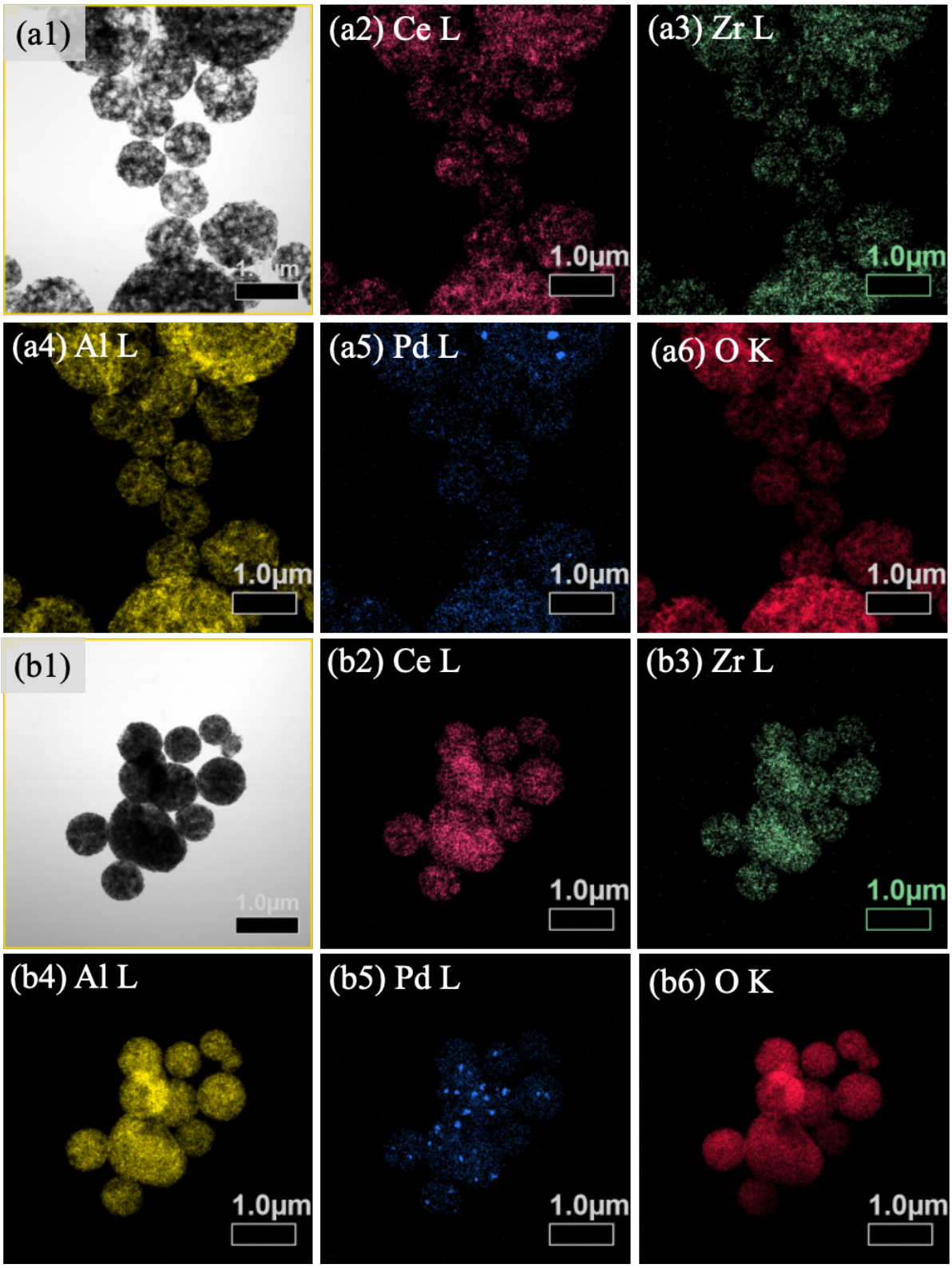

Fig. S9 (a1 and b1) TEM images and (a2-a6 and b2-b6) EDS elemental mapping of (a) 0.5P381-0.5P138 and (b) AGT1 samples for (2) Ce, (3) Zr, (4) Al, (5) Pd, and (6) O.

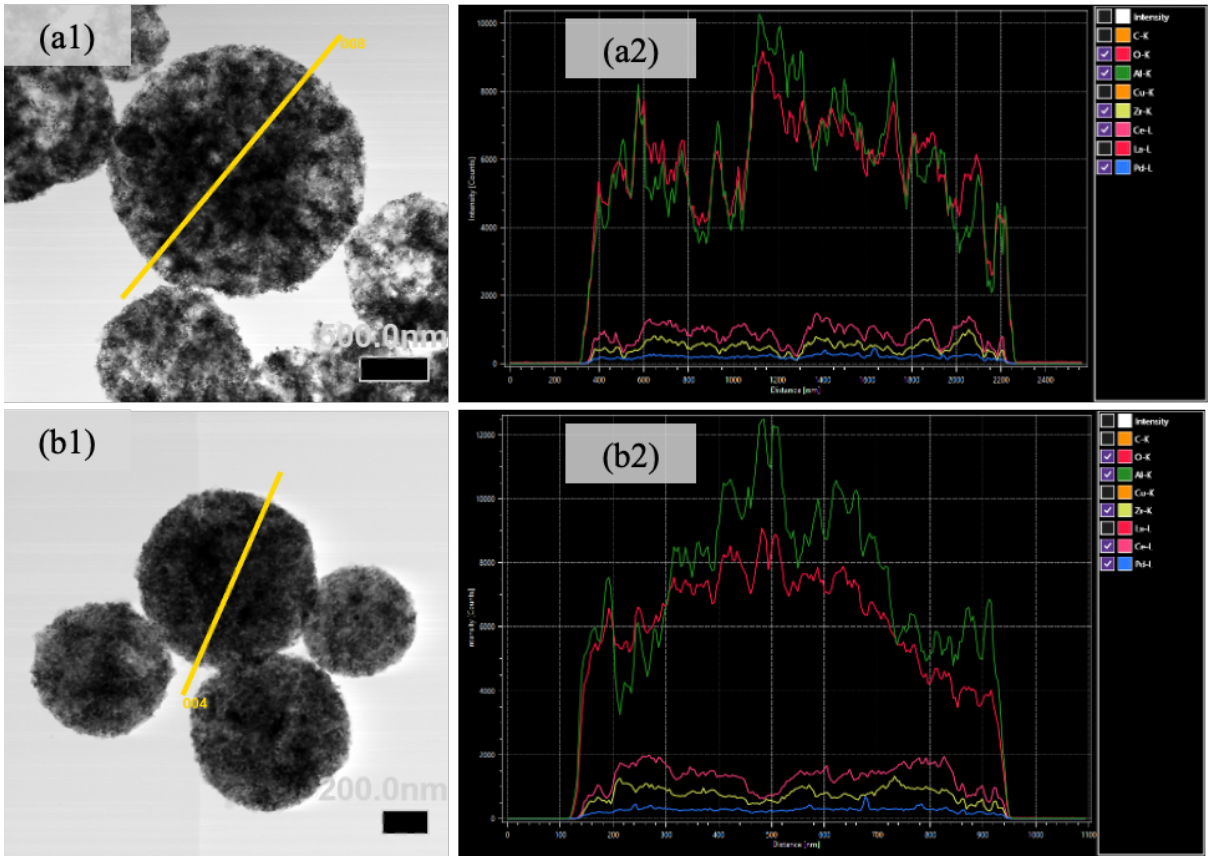

Fig. S10 (a1 and b1) TEM images with an arrow indicating the EDX line scan position and (a2 and b2) EDS line scan of (1) AGT1 and (2) 0.5P381-0.5P138 samples.

10. XRF analysis

The bulk concentration analysis by XRF of the spray-processed nanostructured TWC particles with multiporous, single macroporous, and aggregate structures, represented by 0.5P381–0.5P138, 1P381, and AGT1, respectively, shows that the concentrations of the main oxide supports (Al_2O_3, ZrO_2, CeO_2, La_2O_3, and Nd_2O_3) as well as the active components (PdO and Rh_2O_3) remain consistent with those of the precursor nanoparticles. It should be noted that the elemental concentrations in this analysis were calculated based on the assumption that all elements are present in their oxidized states. **Table S1** shows that the observed variations are minimal, with differences generally within ~1–2% of the specified values. These findings show that spray drying can create nanostructured particles without changing the overall chemical composition of the catalysts. Keeping the composition stable is important because it means the catalysts maintain their activity and durability, even after going through high-temperature processes during synthesis.

Table S1. XRF analysis of the chemical composition of nanostructured TWC particles from 0.5P381-0.5P138, 1P381, and AGT1 samples.

TWC Components	Mass concentration [%]		
	0.5P381-0.5P138	1P381	AGT1
Al_2O_3	48.2	46.6	46.8
ZrO_2	25.4	26.1	26.5
Rh_2O_3	0.26	0.3	0.37
PdO	1.66	1.52	1.68
La_2O_3	3.84	3.52	3.48
CeO_2	17.3	18.2	17.5
Nd_2O_3	2.61	2.64	3.01
HfO_2	0.51	1.06	0.48

11. Mass transfer coefficient of single and multiporous TWC particles

The linear driving force (LDF) approximation was employed to estimate the mass transfer coefficient (k_{LDF}) based on the CO_2 adsorption rates (**Fig. S11**). This coefficient represents the efficiency of molecular transport within the single macroporous and multiporous structure of the TWC particles. To evaluate k_{LDF}, selected uptake rates were analyzed using the LDF model, with a particular focus on low-pressure conditions where mass transport behavior can be more clearly observed. At comparable pressures of 6.8 Pa (single) and 10 Pa (multiporous), the calculated k_{LDF} values reached 41.4×10^{-3} and 62.6×10^{-3}, respectively, as reported in **Table S2**.

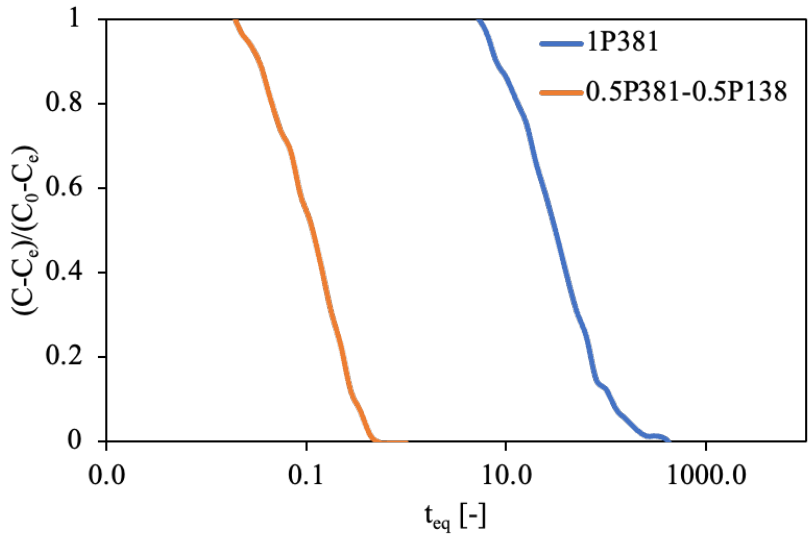

Fig. S11 CO_2 adsorption rates of 1P381 and 0.5P381-0.5P138 samples.

Table S2. Mass transfer coefficients (k_{LDF}) obtained from CO_2 adsorption rates of 1P381 and 0.5P381-0.5P138 samples using Linear Driving Force approximation.

Sample	Pressure [Pa]	k_{LDF} [s^{-1}]
1P381	6.8	41.4×10^{-3}
0.5P381-0.5P138	10	62.6×10^{-3}

12. The stability of multiporous TWC particles

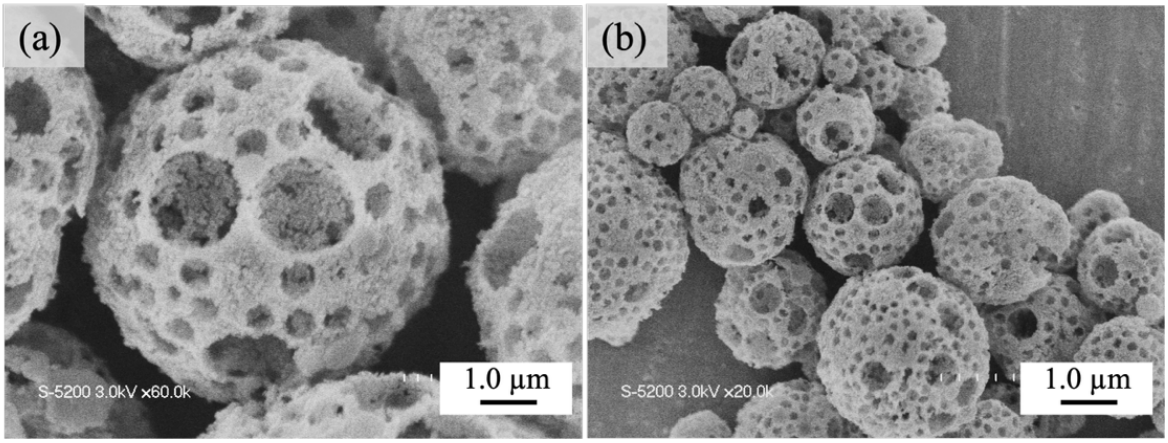

Fig. S12 SEM images of multiporous TWC particles from 0.5P381–0.5P138 sample at (a) high and (b) low magnification after 4 cycles of catalytic testing.

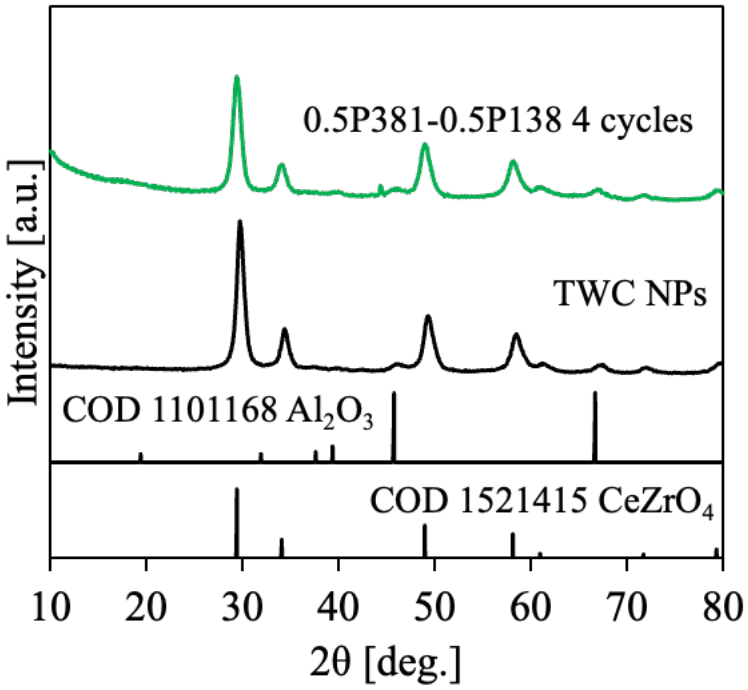

Fig. S13 XRD patterns of 1P381 and 0.5P381-0.5P138 samples after 4 cycles of catalytic testing.

The XPS spectra of the multiporous TWC particles from the 0.5P381–0.5P138 sample were analyzed in the Pd 3d region (**Fig. S14**). In the fresh condition, the catalyst exhibited peaks at 333.3 eV and 337.1 eV, corresponding to Zr $3p_{1/2}$ and PdO, respectively (**Fig. S14a**).

The presence of PdO in the fresh state indicates that palladium predominantly exists in an oxidized form before exposure to the reducing atmosphere. After the reduction treatment in H_2, new metallic Pd^0 signals appeared at 335.5 eV, accompanied by a decrease in the PdO fraction (**Fig. S14b**). This transformation suggests the partial reduction of PdO species to metallic Pd^0, which contributes to the activation of the catalyst surface and enhances its reducibility. Following the CO + O_2 treatment, fluctuations in the relative fractions of Pd^0 and PdO were observed, indicating the occurrence of an oxygen vacancy process within the TWC catalyst (**Fig. S14c**). In addition, the alternating pretreatments with H_2 (reduction) and CO + O_2 (reoxidation) is important to activate and stabilize the Pd–CeO_2 redox cycle for maintaining high CO oxidation activity and long-term catalytic performance in TWC. After four catalytic measurement cycles, the oxidation states of Zr $3p_{1/2}$, Pd^0, and PdO remained relatively stable, with only minor fluctuations (**Fig. S14d**), indicating that the multiporous TWC particles from the 0.5P381–0.5P138 sample preserve their redox properties under repeated reaction conditions.

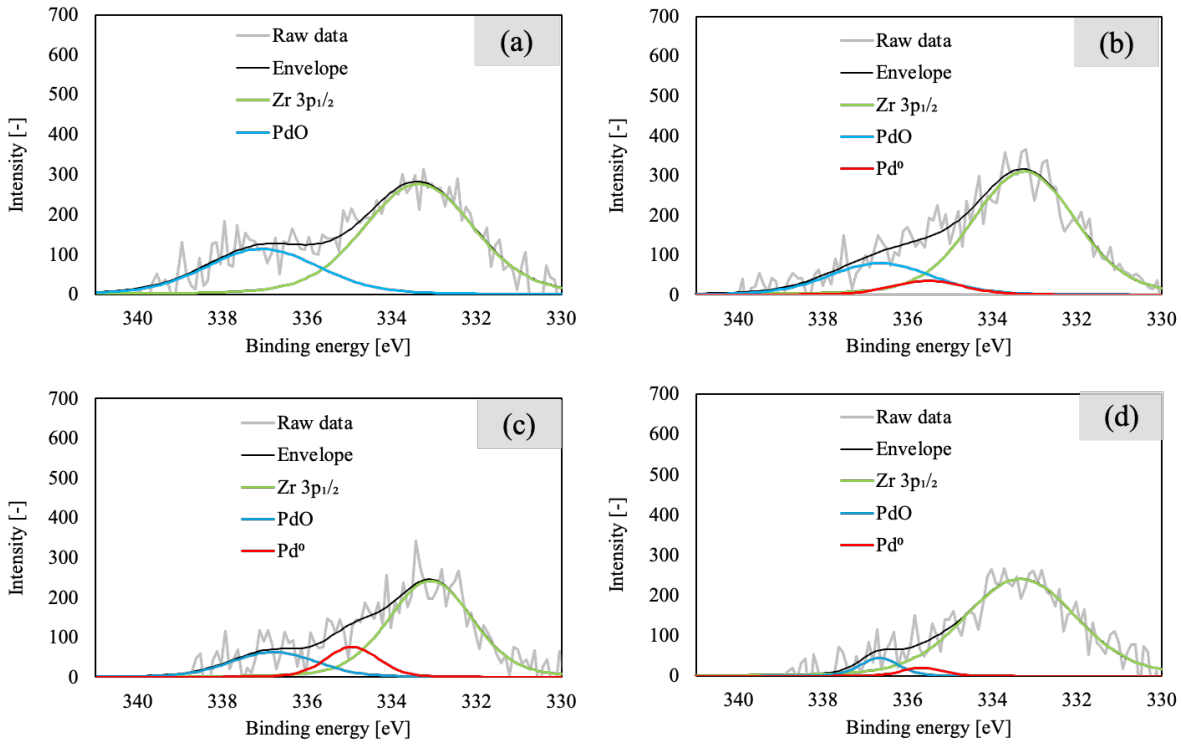

Fig. S14 XPS spectra of multiporous TWC particles at Pd 3d regions for the 0.5P381–0.5P138 sample under (a) fresh condition, (b) after H_2 pretreatment, (c) after CO + O_2 pretreatment, and (d) after four catalytic measurement cycles.

13. Enhanced Mass Transfer in CO Oxidation

The schematic illustration in **Fig. S15** emphasizes that the superior CO oxidation performance of the multiporous TWC particles is closely related to enhanced mass transfer. Generally, the catalytic cycle proceeds through the conventional Pd–CeO_2 redox mechanism (**Fig. S15a**). Initially, CO adsorbs on metallic Pd (I) and reacts with lattice oxygen from CeO_2 to form CO_2 (II), generating oxygen vacancies in the CeO_2 lattice. These vacancies are replenished by molecular O_2, which oxidizes Pd to PdO (III). Subsequently, CO adsorbs again on PdO (IV) and reacts with the coordinated oxygen to produce CO_2, reducing PdO back to Pd while the remaining oxygen fills the CeO_2 vacancies, thus completing the catalytic cycle (V).[7,8] In conventional single macroporous structures (**Fig. S15b**), limited diffusion often slows the replenishment of oxygen vacancies and restricts CO access to interior regions of the catalyst. In contrast, the presence of small and large macropores in multiporous particles (**Fig. S15c**) minimizes diffusion resistance and accelerates the transport of both CO and O_2 molecules throughout the catalyst framework. This structural feature ensures that active sites remain consistently supplied with reactants, thereby sustaining fast redox cycling. Hence, the improved mass transfer enabled by the multiporous architecture is a key factor that distinguishes its catalytic performance from that of conventional single macroporous structures.

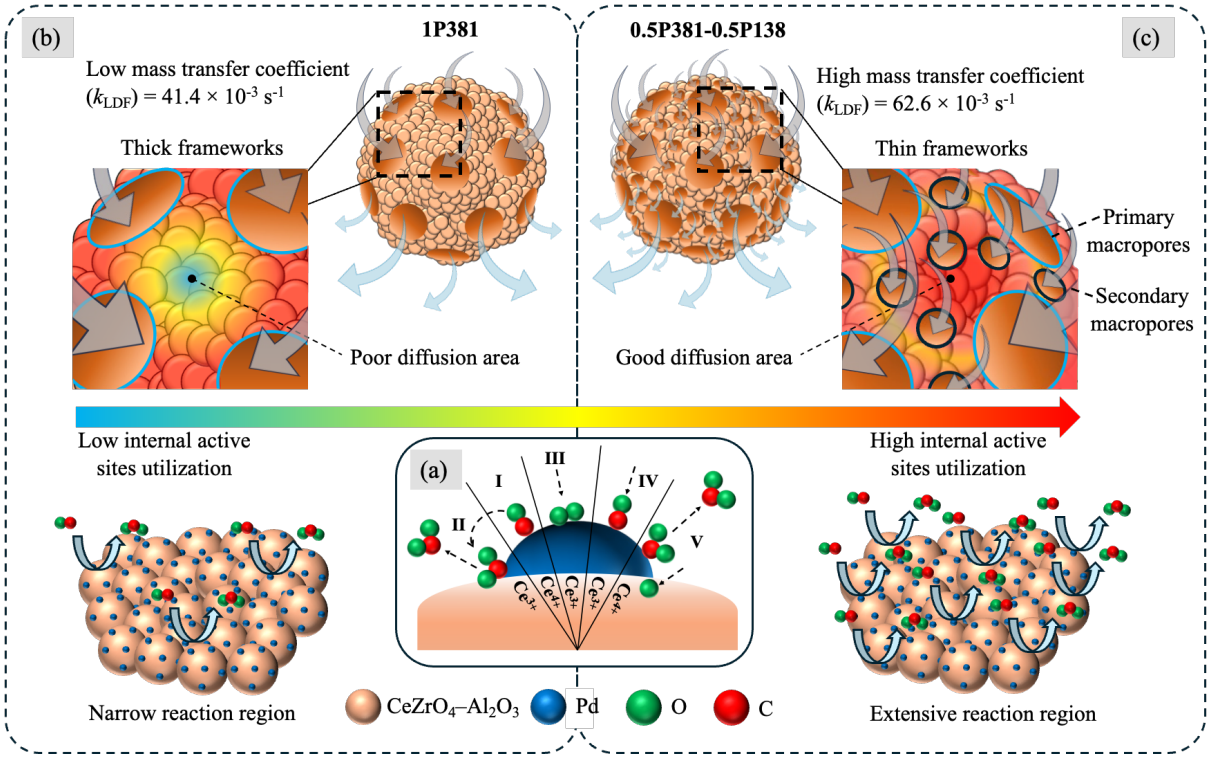

Fig. S15 Schematic image of illustration enhanced catalytic performance of multiporous TWC particles attributed to improved mass transfer during CO oxidation. (a) CO oxidation over the catalyst (b) at low and (c) high mass transfer coefficient.

14. Comparison of CO oxidation rate performances of TWC over different structure

The comparison of catalytic performance across different structural morphologies is summarized in **Fig. S16**, with the corresponding measurement conditions listed in **Table S3**. The results show that multiporous TWC particles exhibit superior catalytic performance compared to nanoparticles, aggregates, and hollow structures. This improvement is attributed to the optimal combination of primary macropores (381 nm) and secondary macropores (138 nm), which effectively reduce framework thickness while maintaining sufficient pore size for reactant penetration. By contrast, introducing smaller secondary pores (61 nm) further decreases the framework thickness (23.4 nm), but the narrow channels restrict gas penetration, as also reported by Suteerapongpun et al.,[9] who observed negligible internal flow in 60 nm PMMA particles. On the other hand, larger secondary pores (242 nm) result in a much thicker framework (151.6 nm), which limits the accessibility of internal active sites, consistent with the findings of Koko et al.,[10] showing that oxygen transport within ceria–zirconia is confined to ~100 nm from the surface. Taken together, these results indicate that the secondary macropores must be sufficiently large (>61 nm) to enable reactant penetration, while the framework thickness must remain below ~100 nm to ensure effective utilization of the internal active sites. In this context, the 138 nm secondary macropores provide the best balance between pore size and framework thickness, enhancing mass transport and utilization of internal active sites.

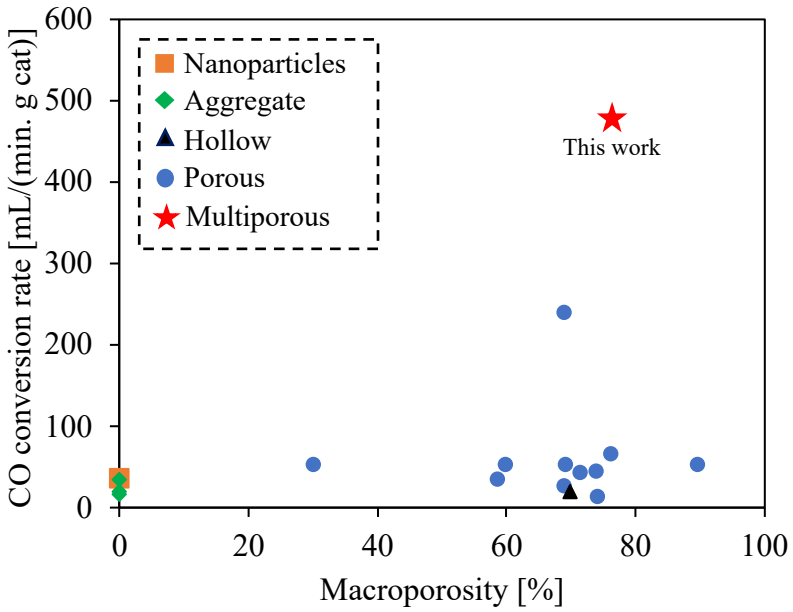

Fig. S16 CO conversion rate performance comparison of TWC particles with multiporous, nanoparticle, aggregate, and hollow structures.

Table S3. Measurement conditions used in the comparative analysis of catalytic performance for multiporous TWC particles and other catalyst structures.

References	TWC particles structure	Template size [nm]	Template concentration [wt%]	Macroporosity [%]	Temperature [°C]	Gas flow rate [mL/min]
[11]	Aggregate	-	-	-	140	50
[11]	Porous	381	1	68.9	140	50
[11]	Porous	381	1	68.9	190	300
[12]	Nanoparticles	-	-	-	130	100
[12]	Aggregate	-	-	-	130	100
[12]	Porous	154	1	30	130	100
[2]	Aggregate	-	-	-	130	100
[2]	Porous	61	1	59.7	130	100
[2]	Porous	138	1	71.2	130	100
[2]	Porous	242	1	58.5	130	100
[2]	Porous	295	1	73.8	130	100
[2]	Porous	381	1	69	130	100
[3]	Porous	368	1	73.9	150	50
[3]	Hollow	334	1	70	150	50
[5]	Porous	360	2	89.4	130	100
This work	Porous	381	1	76	180	300
This work	Multiporous	381 and 138	1[a]	76.4	180	300

[a]Total PMMA concentration 1 wt% (0.5 wt% PMMA 381 nm and 0.5 wt% PMMA138).

References

1 P. H. Le, Y. Kitamoto, K. L. A. Cao, T. Hirano, E. Tanabe and T. Ogi, *Advanced Powder Technology*, 2022, **33**, 103581.

2 P. H. Le, Y. Kitamoto, S. Yamashita, K. L. A. Cao, T. Hirano, T. W. M. Amen, N. Tsunoji and T. Ogi, *ACS Appl Mater Interfaces*, 2023, **15**, 54073–54084.

3 D. B. Kautsar, P. H. Le, A. Ando, K. L. A. Cao, E. L. Septiani, T. Hirano and T. Ogi, *Langmuir*, 2024, **40**, 8260–8270.

4 P. H. Le, K. L. A. Cao, Y. Kitamoto, T. Hirano and T. Ogi, *Langmuir*, 2023, **39**, 7783–7792.

5 D. B. Kautsar, P. H. Le, A. Ando, E. Tanabe, K. L. A. Cao, E. L. Septiani, T. Hirano and T. Ogi, *Nanoscale*, 2025, **17**, 2841–2851.

6 W. Zhang, K. E. Thompson, A. H. Reed and L. Beenken, *Chem Eng Sci*, 2006, **61**, 8060–8074.

7 T. Nagasawa, A. Kobayashi, S. Sato, H. Kosaka, K. Kim, H. Min You, K. Hanamura, A. Terada and T. Mishima, *Chemical Engineering Journal*, 2023, **453**, 139937.

8 W. Song, Y. Su and E. J. M. Hensen, *The Journal of Physical Chemistry C*, 2015, **119**, 27505–27511.

9 T. Suteerapongpun and K. Hanamura, *Membranes (Basel)*, 2023, **13**, 644.

10 P. Koko and K. Hanamura, *Global Journal of Researches in Engineering*, 2023, **23**, 33–42.

11 A. Ando, T. Hirano, K. L. A. Cao, E. L. Septiani, E. Tanabe, R. Ragadhita, A. B. D. Nandiyanto and T. Ogi, *J Colloid Interface Sci*, 2025, **686**, 277–288.

12 P. H. Le, S. Yamashita, K. L. A. Cao, T. Hirano, N. Tsunoji, D. B. Kautsar and T. Ogi, *ACS Appl Nano Mater*, 2023, **6**, 17324–17335.